Permeability and microstructural parameters of 3D-printed triply periodic minimal surface (TPMS) hydroxyapatite scaffolds

Received: 5 April 2025 | Revised: 30 June 2025 | Accepted: 30 June 2025

DOI: 10.1111/jace.70104

Journal of the American Ceramic Society

SPECIAL ISSUE ARTICLE

Permeability and microstructural parameters of 3D-printed triply periodic minimal surface (TPMS) hydroxyapatite scaffolds

Roberta Gabrieli[1] | **Alessandro Schiavi**[2] | **Francesca Romana Pennecchi**[2] | **Dario Alidoost**[1,3] | **Martin Schwentenwein**[4] | **Luca D'Andrea**[5] | **Pasquale Vena**[5] | **Enrica Verné**[1] | **Francesco Baino**[1]

[1]Institute of Materials Physics and Engineering, Department of Applied Science and Technology, Politecnico di Torino, Turin, Italy

[2]Applied Metrology and Engineering Division, National Institute of Metrological Research (INRiM), Turin, Italy

[3]J-Tech Interdepartmental Research Centre, Politecnico di Torino, Turin, Italy

[4]Lithoz GmbH, Vienna, Austria

[5]Laboratory of Biological Structure Mechanics (LaBS), Department of Chemistry, Materials and Chemical Engineering "Giulio Natta", Politecnico di Milano, Milan, Italy

Correspondence
Francesco Baino, Institute of Materials Physics and Engineering, Department of Applied Science and Technology, Politecnico di Torino, Turin, Italy.
Email: francesco.baino@polito.it

Roberta Gabrieli, Martin Schwentenwein, Enrica Verné, and Francesco Baino: Members of the American Ceramic Society (ACerS).

Funding information
European Union—Next Generation EU within the PRIN 2022 program, Grant/Award Number: 104 – 02/02/2022; Ministero dell'Università e della Ricerca), Mission 4, Component 1, CUP, Grant/Award Number: D53D23003390006

Abstract

The search for designing and fabricating truly tissue-like scaffolds is one of the grand challenges in bone tissue engineering. The question on which parameters are actually the most representative of scaffold architecture and, thus, have to be more carefully designed and considered for assessing the scaffold suitability still remains partially open, but permeability and related microstructural parameters show great promise. In this work, we used vat photopolymerization to fabricate three couples of hydroxyapatite scaffolds with different triply periodic minimal surfaces, that are, diamond, gyroid, and I-graph and Wrapped Package (IWP), and for the first time experimentally assessed the Darcian intrinsic permeability of such structures by an acoustic method. Furthermore, we determined the major mass transport properties of these scaffolds (pore tortuosity and pore narrowing ratio) from the microtomographic images of the samples.

KEYWORDS
additive manufacturing, bioceramics, permeability, scaffold, TPMS

1 | INTRODUCTION

Triply periodic minimal surfaces (TPMS) are nature-inspired geometrical entities, which are defined through implicit equations of three-dimensional (3D) spatial coordinates; these surfaces exhibit minimal area and zero-mean curvature.[1] General features of this class of surfaces include their periodicity in three independent directions (hence the name "triply periodic minimal surface"), infinite extension in the 3D space, absence of self-intersections, and capability of splitting the space into two independent labyrinths and zero-mean curvature.[2]

TPMS can be used to generate a regular architecture for bone scaffolds by providing a proper thickness to the surfaces generated by the triply periodicity, thus creating a solid with porosity that can be entirely interconnected, depending on the values of the parameters used for the volume generation.[3]

It was observed that natural trabecular bone exhibits similar properties[4] and, thus, porous implantable scaffolds with TPMS structures are thought to be highly beneficial in optimizing bone regeneration from both biomechanical[5] and morphological viewpoints, being able to promote cell colonization, oxygen diffusion, nutrient transport, and removal of waste substances in a physiological-like way.[6] The interest of researchers toward this group of scaffold geometries is demonstrated by the increasing number of studies published over the last few years[7]; however, most reports are focused on the use of biocompatible polymers, which are relatively easy to process by 3D-printing methods.[8,9] In this regard, perhaps the most important limitation is that TMPS structures can be prepared only by additive manufacturing technologies. This is a particularly challenging task when bioactive ceramics (e.g., hydroxyapatite) and glasses are used for making bone scaffolds due to some issues related to the inherent characteristics of the starting materials and relevant fabrication processes (e.g., reproducibility and reliability of highly porous structures, need for consolidation via high-temperature sintering, printing fidelity).[10,11] Furthermore, although the high osteoconductivity of TPMS hydroxyapatite scaffolds has been convincingly demonstrated,[12] there is a lack of studies focused on the direct comparison between such scaffolds and other porous structures already marketed and used in the clinic.[13]

Compared with random foam materials or lattice arrangement, the TPMS cellular structure is topologically continuous and smooth, thus avoiding structural defects and stress concentrations,[14] which suggest some superiorities from a mechanical viewpoint. However, the overall success of bone scaffolds is strongly dictated by the interaction with body environment and biological fluids, and therefore the pore morphology plays a key role.[15] With specific reference to the scaffold morphology, effective porosity (i.e., the porosity allowing the fluid to flow within the structure), pore size distribution, and pore tortuosity have been recognized as important features which substantially affect the fluid permeability of the scaffolds.[16]

Permeability can be reliably used for quantitative assessment and comparison among different scaffold architectures as well as between porous implant and trabecular bone, and it is responsible for proper mass transport properties that, in turn, dictate the biological performance of the scaffold in vivo.[17] Experimental studies on the permeability of real-scale TMPS scaffolds are scarce in the literature and limited to the analysis of polymeric[18,19] or metallic (e.g., titanium alloy) structures[20] that are fabricated in the form of prototypes having larger size if compared to the real size of implantable devices.

Usually, permeability has also been experimentally measured through liquid-based experiments, for example, pump-based and gravity-based methods, that allow measurement of the pressure drop and the volumetric flow rate through the scaffold using fluid under controlled conditions. Pump-based methods entail the utilization of a perfusion apparatus or a peristaltic pump to force the fluid through the porous sample. This test setup is characterized by a permeability chamber where the scaffold is located and where the pressure drop is measured; deionized water,[21] or air[22] can be used as a fluid medium. Alternatively, a gravity-based system utilizes gravitational force to drive the fluid flow through the scaffold. In this method, the pressure responsible for causing the fluid to flow within the sample is generated by the height difference of the fluid relative to the sample, and no pumps are utilized.[23,24] Typically, in the falling head method, the reservoir fluid level decreases with time and the time between two specific points is recorded; the permeability is then calculated from the fluid height change. On the other hand, in the constant head method, the height of the fluid in the reservoir remains constant, allowing the fluid to flow through the scaffold under a constant pressure head.[25,26]

While these "classical" methods rely on liquid flow and hydrostatic pressure, a different approach has explored alternative measurement principles. In this context, the test bench used for the present study performs a microphone measurement of permeability by detecting the pressure waves drop produced by an oscillating piston that induces alternating airflow through the sample, which is located in a closed cavity of known geometry.[27,28] This approach allows for rapid and reproducible permeability measurements based on an accurate quantification of the acoustic pressure wave, offering an effective alternative option whenever water-based methods are contraindicated for very highly porous or resorbable scaffolds.[16,29]

To the best of the authors' knowledge, this study is the first specifically addressed to the experimental acoustic measurement of permeability in 3D-printed bioceramic (hydroxyapatite) scaffolds with different TPMS structures (diamond, IWP, gyroid) and real-scale size for bone applications, along with the assessment of the major microstructural parameters derived therefrom.

2 | MATERIALS AND METHODS

2.1 | Fabrication of 3D-printed scaffolds

Three TPMS geometries were used to create the scaffolds, based on the analytical formulations reported in ref.[30] Specifically, diamond (D), IWP (I), and gyroid (G) TPMS types were selected and designed with a cylindrical shape (2:1 aspect ratio) and two different levels of total porosity, thereby obtaining six batches of scaffolds in total. The scaffolds were fabricated using the CeraFab 7500 system (Lithoz GmbH), a digital light processing (DLP)-based vat photopolymerization 3D-printing system using a slurry (LithaBone HA480, Lithoz GmbH) composed of hydroxyapatite powder, acrylate/methacrylate-based reactive monomers, dispersing agent, and photoinitiator. After printing, the cleaned green parts were thermally treated to remove the binder and then sintered at 1300°C for 1 h in the same electrical furnace (Nabertherm P330, Nabertherm GmbH). The fabrication process of these hydroxyapatite scaffolds is comprehensively described in a previous work.[31]

2.2 | Tomographic imaging analysis

Microcomputed tomography (micro-CT), conducted by using a custom-made equipment at the Interdepartmental Centre J-Tech of Politecnico di Torino, is a high-resolution technique for the nondestructive analysis of the internal structure of relatively small samples. Micro-CT scans were performed on one sample for each of the six scaffold types, allowing a more detailed analysis of the microarchitecture and porosity. The tomographic system is composed of an X-ray source that generates a focused beam penetrating the sample, while a rotational stage allows the sample to be incrementally rotated for image capture from multiple angles. An X-ray detector captures the attenuated X-rays after they have passed through the sample and converts them into two-dimensional (2D) radiographic projections. Then, a reconstruction software processes the 2D projections using proper algorithms, such as the filtered back-projection, to create a detailed 3D volumetric model of the sample. Projection images were acquired with a source voltage of 100 kV and a source current of 120 μA. The source-to-object distance (SOD) was set to 70 mm, and the source-to-detector distance (SDD) was 1400 mm. No filters were applied, and the angular rotation step was 0.225°, with an acquisition time of 1 s per projection. Postprocessing including the model reconstruction was performed using VGStudio MAX 3.3 software (Volume Graphics). A specific internal subvolume of the scaffold was carefully selected to minimize the artifacts associated with the outer surface, and a dedicated module was then applied to analyze the microstructure of the scaffold within this selected subvolume. The software allowed the segmentation of micro-CT data into topologically disconnected components which could be both visualized and analyzed statistically. Specifically, the volume V_i and surface area S_i of each single pore were quantified; then, the pore true sphericity was calculated as $\varphi_i = \sqrt[3]{36\pi V_i^2}/S_i$[32] and the corresponding equivalent hydraulic average pore diameter was estimated as $D_i = 6V_i/(S_i\varphi_i)$, according to refs.[33,34] for pores of arbitrary shape, under the assumption of a generated and reiterated multisphere particles modeling approach, similar to ref.[35]

2.3 | Microstructural and mass transport features

The fluid flow through a porous medium substantially depends on the microarchitectural properties of the pore space where fluid flows. In particular, pore volume fraction, tortuosity (τ), and pore narrowing ratio (β) affect the overall fluid permeability.[16] As for the porosity, the interconnected open porosity is the effective porosity (ε) that determines the fluid permeability, while dead-end pores will reduce the fluid transport across the sample. The architectures designed for this study are all characterized by fully open porosity, without dead-end pores. However, micro-CT analyses will be carried out to identify printing defects causing pore closures.

The pore tortuosity is a geometrical parameter that indicates how intricate the path of the fluid through the porous media is: the higher the tortuosity, the higher the pressure gradient required to have a given volume flow rate. A higher gradient of pressure is required to overcome the higher energy dissipation due to friction between the fluid and the pore walls; furthermore, a higher tortuosity implies a more frequent change in the direction of the fluid flow; for high-velocity flow (high Reynolds number), leading to inertial effects that decrease the apparent permeability of the medium.

The geometrical definition of the pore tortuosity is:

$$\tau = \frac{L_s}{L_0} \tag{1}$$

in which L_s is the length of the path of the fluid flow along the pore and the shortest distance between the inlet and outlet (i.e., the straight path, L_0). The geometric tortuosity for the six geometries was obtained by applying the method described in ref.[36] The tortuosity of the porous medium is computed by analyzing the micro-CT images of each architecture. In particular, the algorithm searches for connected

paths that start from predefined locations in the first slice in the direction of flow. These locations are the centers of pore bodies in the void space. Once all connected paths are identified, the average length of these paths is used to compute tortuosity as the ratio between the length of the path and the distance between the first slice (the inlet) and the last slice (the outlet). As a result, the number of values of τ correspond to the number of identified paths between the inlet and the outlet. For geometries I1 and I2, characterized by two noncommunicating porous networks, the tortuosity factors were calculated separately for each of the individual porosity.

In order to provide a visual representation of the tortuosity in the TPMS architectures under study, a numerical simulation of the Darcian fluid flow was carried out. The fluid domain of the micro-CT-derived mesh was used to simulate the fluid flow across the cylindrical geometry of scaffolds.[37] The voxel size was 25 μm. Under the hypotheses of rigid solid scaffold and fluid incompressibility, a pressure gradient was imposed between the two end faces of the cylinder, and the resulting fluid flux was computed following the method described in ref.[38] The component of the fluid flux vector aligned with the longitudinal axis of the cylinder was extracted to assess directional flow behavior, and streamlines were generated to visualize the flow direction.

The pore narrowing ratio β is here defined as:

$$\beta = \frac{D_{\max}}{D_t} \tag{2}$$

in which $D_{\max}$ and D_t represent the maximum diameter and the throat diameter of the pores, respectively. The parameter β has been determined for the six geometries applying the geometric definition provided in Equation (2). In a triply periodic structure, β is deterministically obtained by the analytical expression of the surfaces. However, due to the defects introduced in the printing process, the β parameter was calculated on the micro-CT images from real samples. In particular, for each pixel belonging to each fluid path identified for the determination of the tortuosity, the corresponding pore diameter was determined, and the distribution of the fluid channel diameter along all fluid paths was obtained. The pore diameter was determined from micro-CT images as described in ref.[31] The ratio between two consecutive local maximum and minimum along the path determines a sequence of β values for each fluid path. Figure 1 shows the value of the channel radius along one fluid path for the ideal diamond geometry, that is, without printing imperfection (top), and for the real geometry (bottom).

An average value and a standard deviation are eventually obtained for each geometry. For the geometries I1 and I2 that exhibit two separated interconnected porosities, two distinct average values for the pore narrowing ratio were determined.

2.4 | Basic theory behind the experimental assessment of permeability and related measurement

Permeability is influenced by the characteristics of the porous network, such as pore volume, pore size distribution, and pore interconnectivity, with the porosity indeed playing a crucial role in scaffold performance for bone tissue engineering.[39,40] Total porosity represents the fraction of the scaffold volume that is composed of void space (including closed and dead-end pores) and can be quantified using the following equation:

$$\varepsilon = 1 - \frac{\rho_{\text{scaffold}}}{\rho_{\text{material}}} \tag{3}$$

The ratio $\rho_{\text{scaffold}}/\rho_{\text{material}}$ refers to the relative density of the structure. ρ_{material} is the density of the nonporous material of which the scaffold is made and ρ_{scaffold} is the bulk density of the scaffold measured by gravimetric method, dividing its mass (measured using a scale) by its volume (calculated using a caliper). Geometrical parameters (radius and height of each cylindrical scaffold) were assessed as the average of three measurements on each sample.

Several experimental methods are available to measure the intrinsic permeability on the basis of pressure drop and volumetric flow rate through the scaffold.[16] In this study, an acoustic permeameter is used[27] that provides an accurate quantification of the pressure wave drop (measured by a low-pressure-field calibrated microphone) of an alternating very slow airflow through the scaffold, generated by an oscillating piston in a closed cavity. This method allows determining the intrinsic Darcian permeability k_D for oscillating slow flows. At a macroscopic level for linear flows, the intrinsic Darcian permeability k_D is expressed as:

$$k_D = \mu \frac{v}{\Delta P} \times L_0 = \mu \frac{Q_v}{\Delta P} \times \frac{L_0}{A_s} \tag{4}$$

where μ is the dynamic viscosity of the fluid, v is the linear flow velocity, ΔP is the pressure gradient upstream and downstream the scaffold, Q_v is the volumetric linear airflow, L_0 is the length of the porous medium (along the flow direction), A_s is the cross-sectional area of the porous medium perpendicular to the flow direction.

For an oscillating flow, the macroscopic intrinsic Darcian permeability is determined on the basis of the

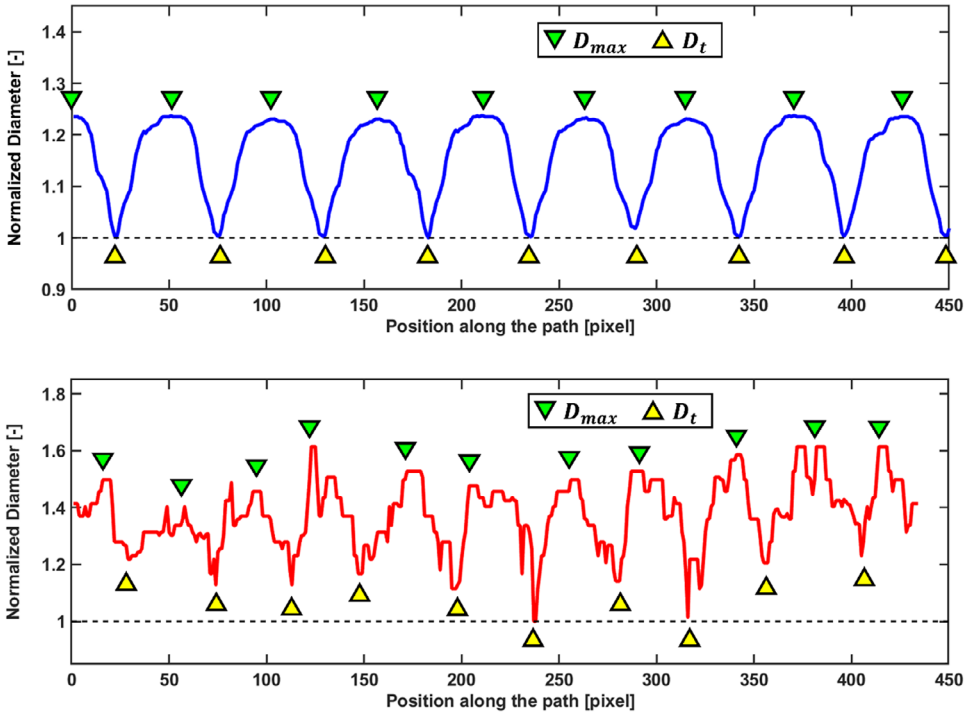

FIGURE 1 Channel diameter along one representative tortuous path. The top panel represents an ideal geometry, whereas the bottom panel a microcomputed tomography (micro-CT) reconstruction. The normalized diameter has been obtained by dividing each diameter by the minimum diameter along the path. Green triangles represent the maximum normalized diameters, whereas yellow triangles the minimum normalized diameters of the throats.

following experimental model[27]:

$$k_D = \mu \frac{\omega V_0}{\gamma p_0} \times \frac{L_0}{A_s} \times \zeta \tag{5}$$

where $q_{v,rms}$ is the alternating r.m.s. volumetric airflow, p_{rms} is the sinusoidal r.m.s. pressure component (depending on the atmospheric static pressure p_0, with heat capacity ratio $\gamma = 1.4$), ∂V is the volume variation induced by the motion of the piston on the volume of air V_0, ω is the angular frequency of the airflow oscillation, and the term ζ is a calibration parameter that depends on the experimental set-up (specifically, it is the ratio between the dynamic pressure waves as measured through the microphone (in mV/Pa_{meas}) and the microphone calibration value (in mV/Pa_{cal}), at the given angular frequency ω). The experiments were conducted with air temperature of 22.8 ± 0.2°C and air viscosity μ of $1.826 \times 10^{-5} \pm 1.175 \times 10^{-8}$ Pa s. The measured constant and linear airflow velocity was $\upsilon \approx 2.4 \times 10^{-2}$ m/s, sufficiently low to ensure laminar flow through the porous scaffolds.

The sensitivity of the acoustic permeameter is established from a direct calibration of the microphone inside the cavity. Results of k_D measurements are supported by a detailed uncertainty budget, determined according to the Guide to the Expression of Uncertainty in Measurement (GUM) along with the related error propagation, as comprehensively discussed in refs.[41,42] The related expanded uncertainty $U(k_D)$ is expressed with a confidence level of 95%, using the following formula:

$$U(k)_{overall} = 2\sqrt{\left(\frac{U(k)_{max}}{2}\right)^2 + \sigma(k)^2} \tag{6}$$

For each TPMS scaffold, the intrinsic permeability was measured on three different samples for three times each, allowing for the calculation of the overall expanded uncertainty for each single TPMS type.

2.5 | Statistics

Traditional statistical analyses based on Gaussian distribution assumption, weighted mean or even fractal modeling, as performed for other kinds of bioceramic scaffolds in previously published papers,[41–43] cannot be applied in the present study because the experimental data distributions of D_p and φ_p show strong skewness and multimodal shape. Actually, these distributions are neither Gaussian, nor symmetric and nor obeying to fractal scaling laws. Therefore, following a completely new approach in the field of

TABLE 1 Geometrical dimensions of triply periodic minimal surfaces (TPMS) scaffolds and total porosity calculated thereof.

	D1	D2	G1	G2	I1	I2
Mean radius R (mm)	3.89 ± 0.01	3.83 ± 0.01	3.55 ± 0.01	3.86 ± 0.02	3.88 ± 0.02	3.90 ± 0.01
Mean height L_0 (mm)	15.55 ± 0.01	15.45 ± 0.01	14.32 ± 0.02	15.65 ± 0.02	16.05 ± 0.02	15.94 ± 0.01
Mean volume V (mm^3)	736.04 ± 2.26	710.46 ± 1.20	565.17 ± 2.67	729.05 ± 3.07	757.77 ± 4.10	762.78 ± 2.00
Total porosity ε (%)	60.0 ± 0.4	51.0 ± 0.4	58.0 ± 0.5	45.0 ± 0.9	50.0 ± 0.6	43.0 ± 0.9

porous bioceramics, we evaluated the typical variability of the average pore diameters on the basis of the median absolute deviation (MAD), which is a robust counterpart estimator to the sample standard deviation for the scale parameter of a distribution.[44] It has the same breakdown point as the median, that is, 50%, whereas the sample standard deviation has the same breakdown point as the sample mean, that is, 0%. The breakdown point of an estimator is the proportion of outliers in a sample of data that the estimator can handle before giving an incorrect result. Then, once defined the median value of the D_i pore diameters as $D_p = \text{median}(D_i)$, the MAD is calculated as:

$$\text{MAD} = \text{median}\left(\left|D_i - D_p\right|\right). \tag{7}$$

From a general viewpoint, in order to use the MAD as a consistent estimator of the distribution standard deviation σ, a normalization is necessary, namely:

$$\hat{\sigma} \cong \frac{\text{MAD}}{0.6745}, \tag{8}$$

where 0.6745 is a scale factor corresponding to $\Phi^{-1}(\frac{3}{4})$, that is, the 75th percentile of a standard normal distribution with cumulative distribution function Φ.[45]

Consistently with the average pore diameter D_p and its variability $\hat{\sigma}(D_p)$, we apply the couple of estimators (median and MAD) to calculate also the average pore sphericity φ_p, along with the corresponding variabilities $\hat{\sigma}(\varphi_p)$.

3 | RESULTS

3.1 | Macroscopic and microstructural features of the scaffolds

Table 1 summarizes the main macrocharacteristics of TPMS scaffolds fabricated in this study, including the geometrical parameters such as mean radius of the basis of the 3D-printed cylindrical scaffold (R), mean height (L_0), mean volume (V) along with their standard deviation, and total porosity (ε), which is determined using Equation (3),

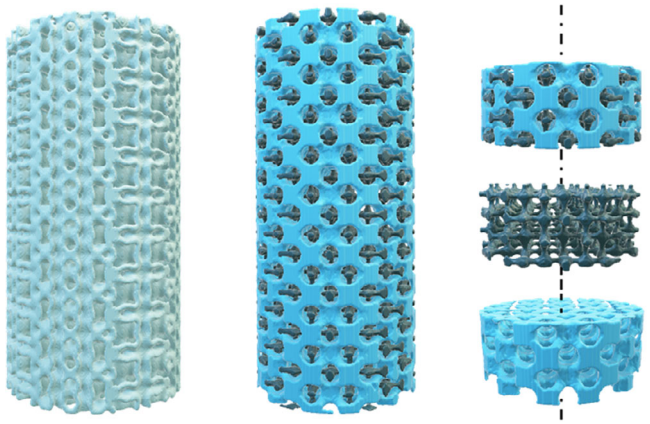

FIGURE 2 The I2 scaffold geometry is shown on the left, while the void fraction (i.e., the empty space or volume of pores) of the scaffold exhibiting two noncommunicating porosities is displayed in the center. On the right side of the figure, an explanation of the two porosities is provided. The primary porosity is represented in blue, while the secondary porosity is depicted in dark blue.

where the nominal density of the hydroxyapatite used for the calculation is 3.16 g/cm^3.

The porosity observed in these samples is consistent with that found in other specimens from the same printing batch as well as with the values estimated by micro-CT analyses and reported elsewhere.[31] Samples D1, D2, and G1 exhibit a fully interconnected porosity, whereas G2, I1, and I2 display two distinct porous networks that remain unconnected. A representation of the porous networks of the I2 is reported in Figure 2 where the two separated pore networks are reported in light blue and dark blue colors in the central and right panels.

As previously reported in ref.,[31] the 3D-printing process tends to reduce wall spacing, which can reduce connectivity when small sizes of samples are involved. This is evident in the G2 geometry (Figure 3), where the secondary porosity is not fully connected (i.e., fluid paths within this pore network do not achieve the outlet section); however, the reduction of the overall porosity is around just 1%, thereby it does not significantly affect the overall effective porosity.

Table 2 shows the average and standard deviation of the tortuosity (τ) and the pore narrowing ratio (β). For the geometries I1 and I2, two different values of τ and β are reported as two separate porosities have been found.

TABLE 2 Mean and standard deviation values of the pore tortuosity and pore narrowing ratio of the six scaffolds.

	D1	D2	G1	G2	I1	I2
$\tau(-)$	1.01 ± 0.01	1.07 ± 0.01	1.02 ± 0.01	1.01 ± 0.01	1.15 ± 0.03 1.01 ± 0.01	1.17 ± 0.04 1.02 ± 0.02
$\beta(-)$	1.33 ± 0.24	1.58 ± 0.41	1.09 ± 0.22	1.08 ± 0.11	1.53 ± 0.26 1.53 ± 0.26	1.72 ± 0.50 1.71 ± 0.51

Two values have been reported for the scaffolds that exhibit a dual porosity.

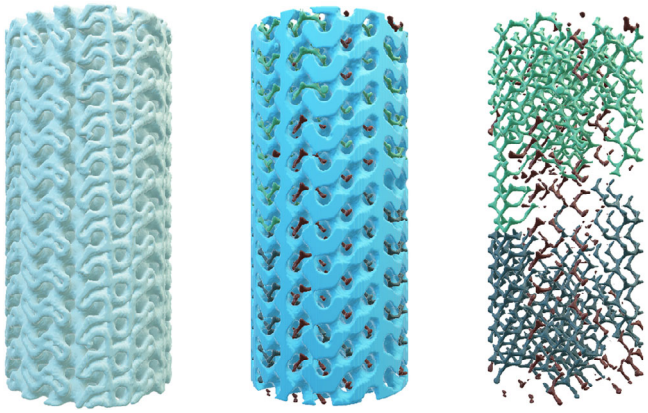

FIGURE 3 The G2 scaffold geometry is shown on the left, while the void fraction (i.e., empty space of pores) of the scaffold exhibiting two noncommunicating porosities is displayed in the center. On the right side of the figure, the interrupted secondary porosity is reported in dark blue, green, and red.

The table shows how the primary porosity of the I1 and I2 geometries exhibited the highest tortuosity, while the highest β is exhibited by I1, I2, and D2. Figure 4 shows the values of τ and β for all fluid paths determined in all geometries. In the left panel, D1 is reported as a representative example (D2, G1, and G2 show similar data distribution); in the right panel, I1 is reported for each of the two separated pore networks (I2 shows a similar data distribution). The right panel clearly shows how the two separated pore networks exhibit similar pore narrowing ratio but substantially different tortuosity. In particular, the secondary porosity (lower porosity with smaller pore size) exhibits a tortuosity close to 1 which is consistent with the straight channel geometry found in the micro-CT (see dark blue pore network in Figure 2). Karaman and Ghahramanzadeh Asl have shown how sheet and network solid structures can be obtained in TPMS architectures by adjusting the numerical parameters of the analytical functions used to generate the structures.[46] Similarly, Figure 4 shows that the D1 geometry is a network solid (as for the D2), whereas the parameters used to generate the I1 and I2 architectures resulted in a sheet solid with two noninterconnected porosity networks. The gyroid structure G1 is a network solid, while G2 is a sheet solid with two unconnected pore networks—one of which (the one with smaller porosity) has closed ends and is therefore ineffective for fluid flow (Figure 3).

Figure 5 illustrates the fluid streamlines traversing the scaffold structures. In the top panel, the D1 geometry is presented, characterized by a single connected porosity. The streamlines closely follow the geometry of the porous network. The histogram in the top right panel shows the distribution of angles between the streamlines and the vertical axis of the cylindrical scaffold obtained at each calculation point; the most frequent value is approximately 25°, reflecting the orientation of the pores. The bottom panels refer to the I1 and I2 geometries which are characterized by two unconnected porosity networks. Each of the two distinct porosities generates a bimodal distribution of streamline angles, which aligns with their respective geometric arrangements. Specifically, the orange histogram reveals two prominent peaks at approximately 0° and 50° reflecting the trajectories of the orange flow path, while the green streamlines exhibit peaks at 0° and 90°. These observations are consistent with the directional characteristics of the corresponding porous domains (see also Figure 2). These results are also consistent with the tortuosity parameters reported in Table 2. Specifically, the I1 and I2 geometries are characterized by two distinct τ values, the higher one referring to the orange path in Figure 5 and the lower one referring to the green path.

3.2 | Experimental determination of intrinsic permeability

The intrinsic permeability k_D of each scaffold was assessed, using the acoustic permeameter, by evaluating the pressure drop of alternating airflow across each cylindrical scaffold under controlled environmental conditions. Table 3 collects the k_D values for each scaffold type, expressed as the overall average, standard deviation, and expanded uncertainty.

The extremely low standard deviation values (two orders of magnitude lower than the average) indicate minimal data dispersion among measurements performed on different scaffolds of the same type. This result demonstrates a high degree of measurement repeatability, confirming that the obtained values are highly consistent with each other.

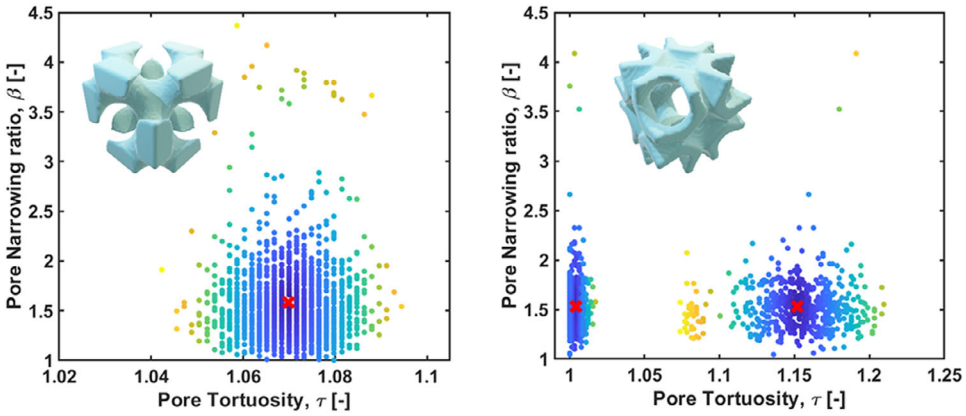

FIGURE 4 Representation of the pore tortuosity and pore narrowing ratio values of two geometries exhibiting two different behaviors. Left panel: D1 geometry exhibits a unique fully connected porosity (D2, G1, and G2 exhibit similar behaviors). Right panel: I1 geometry exhibits two clusters of data, representing the two porosities (I2 exhibits similar behavior). For both panels, the color gradient represents the distance between the average value (red cross) and the single data point.

TABLE 3 Darcian permeability of the six triply periodic minimal surfaces (TPMS) scaffold types along with the relevant uncertainty.

	D1	D2	G1	G2	I1	I2
Intrinsic permeability average k_D (m^2)	1.37×10^{-9}	1.20×10^{-9}	1.07×10^{-9}	1.45×10^{-9}	5.68×10^{-10}	5.81×10^{-10}
Intrinsic permeability standard deviation $\sigma(k_D)$ (m^2)	6.17×10^{-11}	2.99×10^{-11}	2.72×10^{-11}	6.41×10^{-11}	1.75×10^{-11}	2.12×10^{-11}
Overall expanded uncertainty $U(k_D)_{overall}$ (m^2)	2.16×10^{-10}	1.41×10^{-10}	7.98×10^{-11}	1.74×10^{-10}	6.79×10^{-11}	4.70×10^{-11}

Figure 6 shows how the two microstructural parameters τ and β affect the overall permeability of the scaffolds.

Specifically, the left panel of Figure 6 shows how porosity and tortuosity affect the permeability; lower porosity in general implies higher tortuosity and lower permeability (brighter gray color), with the exception of G2. The right panel of Figure 6 shows how the increase of the narrowing ratio slightly decreases the permeability, with the exception of G2 that exhibited a substantially higher permeability.

3.3 | Analysis of pores

Micro-CT analysis of the reconstructed volumes allowed for determining the distributions of the pore diameter and pore sphericity of each single scaffold analyzed in the present study. According to the MAD-based statistical analysis described in Section 2.5, the overall statistical results are summarized in Table 4.

A graphical representation of the statistical estimators for the pore diameter is also displayed in Figure 7. The median values and the ranges [median ± normalized MAD] (pink boxes) are illustratively combined with the traditional boxplot, including outliers, arithmetic mean values, and the interquartile range (IQR).

The variability of pore diameter values and pore sphericity values, included in the range identified by the normalized MAD (pink boxes), can be considered representative of the actual size and shape of the pores in the scaffolds here investigated.

4 | DISCUSSION

The experimental results obtained in the present study provide valuable insights into permeability and microstructural characteristics of 3D-printed hydroxyapatite scaffolds with TPMS structures. The use of diamond, gyroid, and IWP surfaces allowed for a quantitative comparison of permeability values across different TPMS types, providing a deeper understanding of how pore characteristics may influence fluid transport.

The TPMS scaffolds designed for this study are characterized by fully interconnected porosity,[9,47,48] which is a key requirement for bone tissue engineering applications ensuring cell penetration, nutrient exchange, and vascularization.[15,49–52] The total porosity of the 3D-printed scaffolds varied between 0.43 and 0.60, values that lie in the range reported for human trabecular bone.[53] The pore diameter of each TPMS type reveals that the pore sizes are in the range of few hundred micrometres.[31,54] These

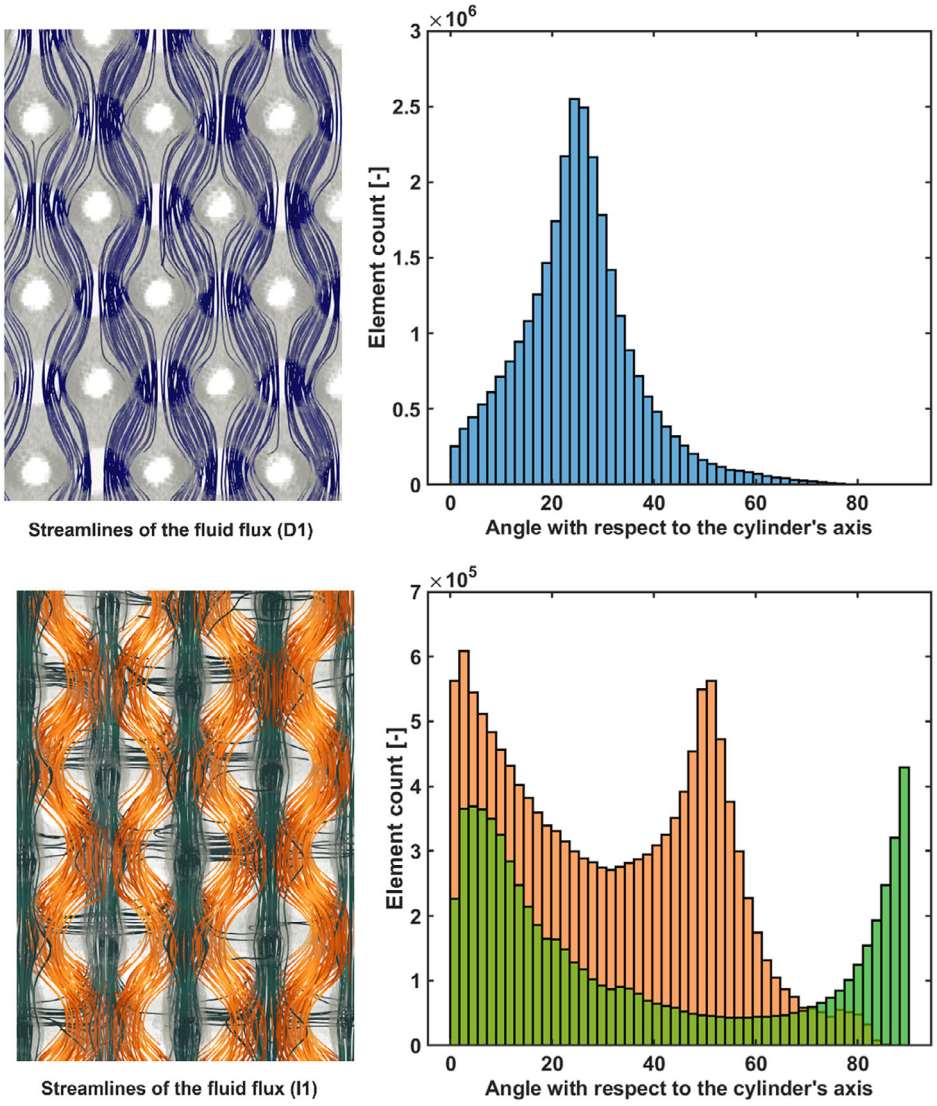

FIGURE 5 Representation of the fluid flux streamlines (left) and histograms of the fluid flux vector orientation (right) of two geometries exhibiting two different behaviors. Top panel: D1 geometry exhibits a unique fully connected porosity (D2, G1, and G2 exhibit similar behaviors). Bottom panel: I1 geometry exhibits two noncommunicating porosities, thereby the streamlines do not intersect themselves. Note that the streamlines were projected on a planar view, even if they evolve in the three-dimensional (3D) space.

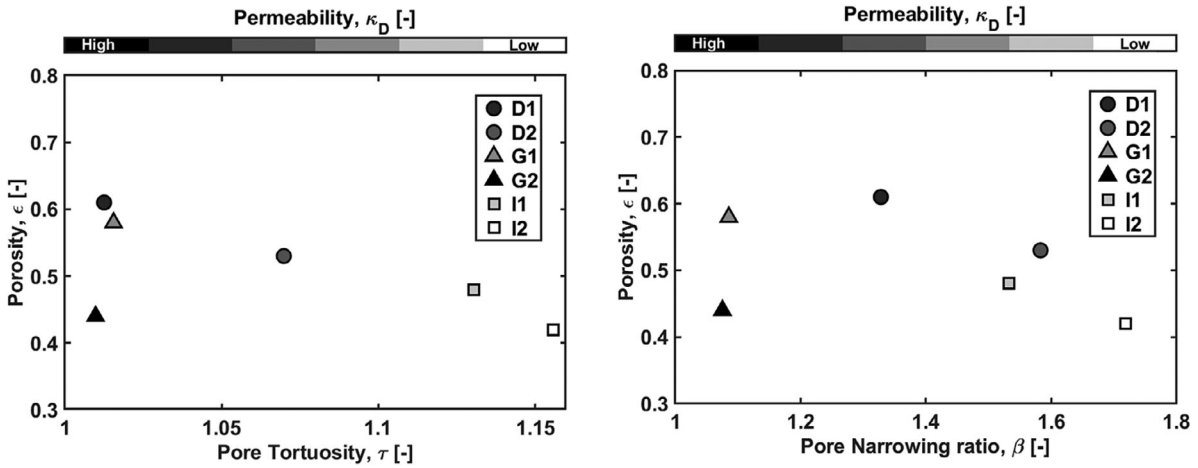

FIGURE 6 Left panel: dependency of the porosity with respect to the tortuosity. Right panel: dependency of the porosity with respect to the pore narrowing ratio.

TABLE 4 Statistical analysis for pore size and sphericity deriving from the median absolute deviation (MAD)-based approach.

	D1	D2	G1	G2	I1	I2
Median pore diameter D_p (μm)	713.56	770.37	585.24	599.77	756.60	1077.51
Normalized MAD $\hat{\sigma}(D_p)$ (μm)	139.78	160.10	108.78	257.48	245.4	178.03
Median pore sphericity φ_p (−)	0.45	0.42	0.43	0.45	0.42	0.32
Normalized MAD $\hat{\sigma}(\varphi_p)$ (−)	0.06	0.07	0.04	0.05	0.12	0.10

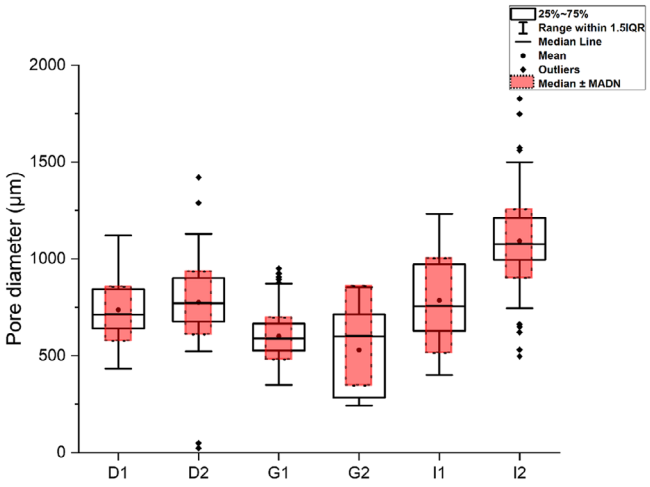

FIGURE 7 Statistical estimators of pore diameters.

values are in the range of the pore size well accepted for bone tissue engineering applications.[54–59] The permeability values obtained in this study can be compared with the results reported in the literature for other hydroxyapatite scaffolds produced by the same DLP-based vat photopolymerization method and measured through the same equipment. The Darcian permeability of foam-like hydroxyapatite scaffolds (1.25×10^{-9} m^2)[28,42] is comparable to that of diamond and gyroid structures, while the values for IWP type are lower of around 50% (see Table 3). Permeability values obtained using a pump-based method for hydroxyapatite foam-like cylinders (0.4×10^{-9}–3.24×10^{-9} m^2)[60] are in the same range of value of those obtained in this study. Biphasic calcium phosphate scaffolds with double-gyroid architecture creating a gradient of porosity exhibited permeability values (experimentally assessed by using water as a flowing medium) in the range of 4×10^{-9} to 8×10^{-9} m^2; however, computational results for the same scaffolds were significantly higher (12×10^{-9}–22×10^{-9} m^2).[24] Indeed, a comparison among all these cases is difficult and the variability of the results reported may depend on the different measurement methods as well on the different porous architecture of the samples tested; these important methodological issues have been discussed elsewhere in a critical review.[16] It is important to note, however, that natural bone permeability may exhibit a significant variability even within the same anatomical site; furthermore, other factors such as sex and age (often combined together like in osteoporosis, which is prevalent in women over 60[61]) have an impact on bone microstructure and, hence, permeability. Overall, the values measured in the present study lie within the range published by Nauman et al.[62] and Grimm and Williams[63] for human bone permeability, reinforcing the reliability of our experimental findings and their validity concerning physiological conditions. Quantitative analysis by micro-CT also allowed gaining further in-depth microstructural information. In particular, tortuosity and pore narrowing in the pore networks have been quantitatively evaluated.

Indeed, the pore narrowing ratios of these TPMS structures are definitely lower than the range reported for foam-like hydroxyapatite scaffolds produced by the same 3D-printing method in a previous work (2.176–2.727).[42] The discrepancy is due to the different architectures studied in the present previous study.[42] The β parameter is an indication of the narrowing throats encountered by the fluid fillets along their paths; these narrowing walls will impress trajectory variations to the fluid fillets thus introducing inertial effects in the overall permeability of the porous material. Furthermore, pore narrowing over a short length of fluid path also induced head loss also impacting the overall permeability. In laminar slow flows with low Reynolds numbers, these effects are negligible, making the β parameter of limited interest for fluid dynamics within the scaffolds. However, the β parameter may have a substantial impact of the wall shear stress and eventually on the cell mechanical stimulus and cell proliferation within the scaffolds.

It is worth noting that the tortuosity parameter determined on the geometry of the fluid path is a lower limit of the actual tortuosity of the fluid fillets. The method applied in this study searches for all possible connected pixels in each subsequent slice and eventually selects the shortest path found in a single channel; this implies that the paths follow the shortest path in a curved channel, while fluid fillets will probably follow more paths, including longer ones. Although the simulation of the Darcian fluid flow presented in Figure 5 already gives an indication of the geometrical path of the fluid, a computational fluid dynamics (CFD) simulation would be required to correctly identify the real tortuosity. In ref.,[64] the tortuosity parameters obtained through CFD for the diamond, IWP, and

gyroid architectures were 1.325, 1.051, and 1.256, respectively. These values are slightly higher (for the diamond and gyroid) if compared to those reported in Table 2. The discrepancy is due to two major factors: (i) lower porosity are considered in ref.[64] and (ii) the different methods used to estimate the parameter. As shown in Figure 5, G2 exhibited the highest permeability despite having a relatively lower porosity if compared to G1. It can be speculated that the pore narrowing ratio and tortuosity play a role prevailing on the effect given by the overall porosity. Indeed, G2 exhibited a higher pore size and lower tortuosity size in comparison to G1.[31]

5 | CONCLUSIONS

This work reports, for the first time, the experimental measurement and comparison of Darcian permeability in TPMS bioceramics scaffolds with diamond, gyroid, and IWP structures. The experimental method to determine permeability was proved to be effective for small-size ceramic bone scaffolds with TPMS architecture. The permeability values have been analyzed in correlation with major microstructural parameter, especially effective porosity, tortuosity, and pore narrowing ratio, revealing that the porosity parameter alone is not sufficient to characterize permeability properties. Diamond and gyroid scaffolds, being associated with higher permeability values, show better promise for bone tissue engineering applications from the viewpoint of architectural suitability, if bone permeability is assumed as a selection criterion.

ACKNOWLEDGMENTS

This study was partially carried out within the project artificial intelligence-based design of 3D PRINTed scaffolds for the repair of critical-sized BONE defects I-PRINT-MY-BONE funded by European Union—Next Generation EU within the PRIN 2022 program (D.D. 104 – 02/02/2022 Ministero dell'Università e della Ricerca), Mission 4, Component 1, CUP D53D23003390006.

Open access publishing facilitated by Politecnico di Torino, as part of the Wiley - CRUI-CARE agreement.

CONFLICT OF INTEREST STATEMENT

The authors declare no conflicts of interest.

REFERENCES

1. Gupta A, Babu L S. Triply periodic minimal surfaces: an overview of their features, failure mechanisms, and applications. J Mines Metals Fuels. 2023;70:211–21. https://doi.org/10.18311/jmmf/2022/31230
2. Rajagopalan S, Robb R. Schwarz meets Schwann: design and fabrication of biomorphic and durataxic tissue engineering scaffolds. Med Image Anal. 2006;10:693–712. https://doi.org/10.1016/j.media.2006.06.001
3. Restrepo S, Ocampo S, Ramírez JA, Paucar C, and García C. Mechanical properties of ceramic structures based on triply periodic minimal surface (TPMS) processed by 3D printing. J Phys Conf Ser. 2017;935:012036. https://doi.org/10.1088/1742-6596/935/1/012036
4. Jinnai H, Watashiba H, Kajihara T, Nishikawa Y, Takahashi M, and Ito M. Surface curvatures of trabecular bone microarchitecture. Bone. 2002;301:191–94. https://doi.org/10.1016/S8756-3282(01)00672-X
5. Guo X, Zheng X, Yang Y, Yang X, and Yi Y. Mechanical behavior of TPMS-based scaffolds: A comparison between minimal surfaces and their lattice structures. SN Appl Sci. 2019;1(10):1145. https://doi.org/10.1007/s42452-019-1167-z
6. Sanjairaj V, Zhang L, Zhang S, Fuh J, and Lu W. Triply periodic minimal surfaces sheet scaffolds for tissue engineering applications: an optimization approach toward biomimetic scaffold design. ACS Appl Bio Mater. 2018;1(2):259–69. https://doi.org/10.1021/acsabm.8b00052
7. Ma J, Li Y, Mi Y, Gong Q, Zhang P, Meng B, et al. Novel 3D printed TPMS scaffolds: microstructure, characteristics and applications in bone regeneration. J Tissue Eng. 2024;15:20417314241263689. https://doi.org/10.1177/20417314241263689
8. Diez-Escudero A, Harlin H, Isaksson P, and Persson C. Porous polylactic acid scaffolds for bone regeneration: a study of additively manufactured triply periodic minimal surfaces and their osteogenic potential. J Tissue Eng. 2020;11:204173142095654, https://doi.org/10.1177/2041731420956541
9. Gabrieli R, Wenger R, Mazza M, Verné E, and Baino F. Design, stereolithographic 3D printing, and characterization of TPMS scaffolds. Materials. 2024;17(3):654. https://doi.org/10.3390/ma17030654
10. D'Andrea L, Gastaldi D, Baino F, Verné E, Schwentenwein M, Örlygsson G et al. Computational models for the simulation of the elastic and fracture properties of highly porous 3D-printed hydroxyapatite scaffolds. Int J Numer Method Biomed Eng. 2024;40(2):e3795. https://doi.org/10.1002/cnm.3795
11. Baino F, Gaido F, Gabrieli R, Alidoost D, Schiavi A, Mohammadi M, et al. Vat photopolymerization of ultra-porous bioactive glass foams. Open Ceram. 2024;20:100690. https://doi.org/10.1016/j.oceram.2024.100690
12. Maevskaia E, Khera N, Ghayor C, Bhattacharya I, Guerrero J, Nicholls F, et al. Three-dimensional printed hydroxyapatite bone substitutes designed by a novel periodic minimal surface algorithm are highly osteoconductive. 3D Print Addit Manuf. 2023;10(5):905–16. https://doi.org/10.1089/3dp.2022.0134
13. Hing K, Best S, and Bonfield W. Characterization of porous hydroxyapatite. J Mater Sci Mater Med. 1999;10:135–45. https://doi.org/10.1023/A:1008929305897
14. Maskery I, Sturm L, Aremu A, Panesar A, Williams C, Tuck C, et al. Insights into the mechanical properties of several triply periodic minimal surface lattice structures made by polymer additive manufacturing. Polymer (Guildf). 2018;152:62–71. https://doi.org/10.1016/j.polymer.2017.11.049
15. Karageorgiou V, Kaplan D. Porosity of 3D biomaterial scaffolds and osteogenesis. Biomaterials. 2005;2627:5474–91. https://doi.org/10.1016/j.biomaterials.2005.02.002

16. Gabrieli R, Schiavi A, and Baino F. Determining the permeability of porous bioceramic scaffolds: significance, overview of current methods and challenges ahead. Materials. 2024;17(22):5522. https://doi.org/10.3390/ma17225522
17. Mitsak AG, Kemppainen JM, Harris MT, and Hollister SJ. Effect of polycaprolactone scaffold permeability on bone regeneration in vivo. Tissue Eng Part A. 2011;17(13–14):1831–39. https://doi.org/10.1089/ten.tea.2010.0560
18. Montazerian H, Zhianmanesh M, Davoodi E, Milani AS, and Hoorfar M. Longitudinal and radial permeability analysis of additively manufactured porous scaffolds: effect of pore shape and porosity. Mater Des. 2017;122:146–56. https://doi.org/10.1016/j.matdes.2017.03.006
19. Pires T, Santos J, Ruben R, Gouveia B, Castro A, and Fernandes P. Numerical-experimental analysis of the permeability-porosity relationship in triply periodic minimal surfaces scaffolds. J Biomech. 2021;117:110263. https://doi.org/10.1016/j.jbiomech.2021.110263
20. Yánez A, Cuadrado A, Martel O, Fiorucci M, and Deviaene S. Mechanical and permeability properties of skeletal and sheet triply periodic minimal surface scaffolds in bone defect reconstruction. Results Eng. 2024;21:101883. https://doi.org/10.1016/j.rineng.2024.101883
21. Ochoa I, Sanz-Herrera JA, García-Aznar JM, Doblaré M, Yunos DM, and Boccaccini AR. Permeability evaluation of 45S5 Bioglass®-based scaffolds for bone tissue engineering. J Biomech. 2009;42(3):257–60. https://doi.org/10.1016/j.jbiomech.2008.10.030
22. Chor MV, Li W. A permeability measurement system for tissue engineering scaffolds. Meas Sci Technol. 2007;18(1):208. https://doi.org/10.1088/0957-0233/18/1/026
23. Dias MR, Fernandes PR, Guedes JM, and Hollister SJ. Permeability analysis of scaffolds for bone tissue engineering. J Biomech. 2012;45(6):938–44. https://doi.org/10.1016/j.jbiomech.2012.01.019
24. Wang Y Liu Y, Chen S, Francis Siu MF, Liu C, Bai J, et al. Enhancing bone regeneration through 3D printed biphasic calcium phosphate scaffolds featuring graded pore sizes. Bioact Mater. 2025;46:21–36. https://doi.org/10.1016/j.bioactmat.2024.11.024
25. Bagarello V, Iovino M, and Elrick DE. A simplified falling-head technique for rapid determination of field-saturated hydraulic conductivity. Soil Sci Soc Am J—SSSAJ. 2004;68:66–73. https://doi.org/10.2136/sssaj2004.0066
26. Asha SA. Comparison of permeability in constant head and falling head method: comparison of permeability in constant head and falling head method and establishment of empirical relationship between them. Saarbrucken, Germany: LAP Lambert Academic Publishing; 2010.
27. Schiavi A, Guglielmone C, Pennella F, and Morbiducci U. Acoustic method for permeability measurement of tissue-engineering scaffold. Meas Sci Technol. 2012;23:105702. https://doi.org/10.1088/0957-0233/23/10/
28. Baino F, Magnaterra G, Fiume E, Schiavi A, Tofan L-P, Schwentenwein M, et al. Digital light processing stereolithography of hydroxyapatite scaffolds with bone-like architecture, permeability, and mechanical properties. J Am Ceram Soc. 2021;105:1648–57. https://doi.org/10.1111/jace.17843
29. Fiume E, Schiavi A, Orlygsson G, Bignardi C, Verné E, and Baino F. Comprehensive assessment of bioactive glass and glass-ceramic scaffold permeability: experimental measurements by pressure wave drop, modelling and computed tomography-based analysis. Acta Biomater. 2021;119:405–18. https://doi.org/10.1016/j.actbio.2020.10.027
30. Ibrahimi S, D'Andrea L, Gastaldi D, Rivolta M, and Vena P. Machine learning approaches for the design of biomechanically compatible bone tissue engineering scaffolds. Comput Methods Appl Mech Eng. 2024;423:116842. https://doi.org/10.1016/j.cma.2024.116842
31. D'Andrea L, Gabrieli, R, Milano, L, Magagnin, L, De Cet, A, Alidoost, D, et al. Elastic and failure characterization of hydroxyapatite TPMS scaffolds using a combined approach of ultrasound, compression tests and micro-CT based numerical models. Acta Mater. 2025;287:120776. https://doi.org/10.1016/j.actamat.2025.120776
32. Wadell H. Volume, shape, and roundness of rock particles. J Geol. 1932;40(5):443–51. https://doi.org/10.1086/623964
33. Leva M, Weintraub M, Grummer M, Pollchik M, and Sforch HH. Bulletin 504. United States Bureau of Mines. Fluid flow through packed and fluidized systems. 1951. https://digital.library.unt.edu/ark:/67531/metadc12663/. Accessed 30 Jun 2025 [Online].
34. Niven R. Physical insight into the Ergun and Wen and Yu equations for fluid flow in packed and fluidized beds. Chem Eng Sci. 2002;57:527–34. https://doi.org/10.1016/S0009-2509(01)00371-2
35. Angelidakis V, Nadimi S, Otsubo M, and Utili S. CLUMP: a code library to generate universal multi-sphere particles. SoftwareX. 2021;15:100735. https://doi.org/10.1016/j.softx.2021.100735
36. Al-Raoush RI, Madhoun IT. TORT3D: a MATLAB code to compute geometric tortuosity from 3D images of unconsolidated porous media. Powder Technol. 2017;320:99–107. https://doi.org/10.1016/j.powtec.2017.06.066
37. Cooper SJ, Bertei A, Shearing PR, Kilner JA, and Brandon NP. TauFactor: an open-source application for calculating tortuosity factors from tomographic data. SoftwareX. 2016;5:203–10. https://doi.org/10.1016/j.softx.2016.09.002
38. D'Andrea L, Goretti G, Magrini G, and Vena P. Tuning the trabecular orientation of Voronoi-based scaffold to optimize the micro-environment for bone healing. Biomech Model Mechanobiol. 2025;24:1057–71. https://doi.org/10.1007/s10237-025-01953-8
39. Ashworth JC, Best SM, and Cameron RE. Quantitative architectural description of tissue engineering scaffolds. Materials Technology. 2014;29:5. https://doi.org/10.1179/1753555714Y.0000000159
40. Zheng J, Zheng L, Liu H, and Ju Y. Relationships between permeability, porosity and effective stress for low-permeability sedimentary rock. Int J Rock Mech Mining Sci. 2015;78:304–18. https://doi.org/10.1016/j.ijrmms.2015.04.025
41. Schiavi A, Gabrieli R, Orlygsson G, Schwentenwein M, Verné E, and Baino F. Assessment of permeability and microstructural parameters via fractal modelling in bioactive glass-derived scaffolds produced by vat photopolymerization. J Eur Ceram Soc. 2024;44(7):4689–98. https://doi.org/10.1016/j.jeurceramsoc.2024.01.095
42. Schiavi A, Fiume E, Orlygsson G, Schwentenwein M, Verné E, and Baino F. High-reliability data processing and calculation of microstructural parameters in hydroxyapatite scaffolds

produced by vat photopolymerization. J Eur Ceram Soc. 2022; 42(13):6206–12. https://doi.org/10.1016/j.jeurceramsoc.2022.06.022
43. Schiavi A, Gaido F, Gabrieli R, Alidoost D, Schwentenwein M, Mohammadi M, et al. Permeability and tomography-based microstructural analysis of ultra-porous bioactive glass scaffolds. Mater Lett. 2025;384:138064. https://doi.org/10.1016/j.matlet.2025.138064
44. Huber PJ. Robust statistics. Wiley Series in Probability and Statistics; 1981. https://doi.org/10.1002/0471725250
45. Rousseeuw PJ, Croux C. Alternatives to the median absolute deviation. J Am Stat Assoc. 1993;88(424):1273–83. https://doi.org/10.1080/01621459.1993.10476408
46. Karaman D, Ghahramanzadeh Asl H. The effects of sheet and network solid structures of similar TPMS scaffold architectures on permeability, wall shear stress, and velocity: a CFD analysis. Med Eng Phys. 2023;118:104024. https://doi.org/10.1016/j.medengphy.2023.104024
47. Kowalczyk P, Furmaniak S, Neimark A, Burian A, and Terzyk A. Surface-constrained metropolis Monte Carlo: simulation of reactions on triply periodic minimal surfaces. J Phys Chem A. 2024;128(9):1725–35. https://doi.org/10.1021/acs.jpca.3c08203
48. Ma J, Li Y, Mi Y, Gong Q, Zhang P, Meng B, et al. Novel 3D printed TPMS scaffolds: microstructure, characteristics and applications in bone regeneration. J Tissue Eng. 2024;15: 20417314241263689. https://doi.org/10.1177/20417314241263689
49. Roseti L, Parisi V, Petretta M, Cavallo C, Desando G, Bartolotti I, et al. Scaffolds for bone tissue engineering: state of the art and new perspectives. Mater Sci Eng: C. 2017;78:1246–62. https://doi.org/10.1016/j.msec.2017.05.017
50. Amini AR, Laurencin CT, and Nukavarapu SP. Bone tissue engineering: recent advances and challenges. Crit Rev Biomed Eng. 2012;40(5):363–408. https://doi.org/10.1615/critrevbiomedeng.v40.i5.10
51. Lee S, Du X, Kim I, and Ferguson S. Scaffolds for bone-tissue engineering. Matter. 2022;5:2722–59. https://doi.org/10.1016/j.matt.2022.06.003
52. Yu T, Liu Q, Jiang T, Wang X, Yang Y, and Kang Y. Channeled β-TCP scaffolds promoted vascularization and bone augmentation in mandible of beagle dogs. Adv Funct Mater. 2016;26(37):6719–27. https://doi.org/10.1002/adfm.201602631
53. Morgan EF, Unnikrisnan GU, and Hussein AI. Bone mechanical properties in healthy and diseased states. Annu Rev Biomed Eng. 2018;20:119–43. https://doi.org/10.1146/annurev-bioeng-062117-121139
54. Abbasi N, Hamlet S, Love RM, and Nguyen N. Porous scaffolds for bone regeneration. J Sci: Adv Mater Devices. 2020;5(1):1–9. https://doi.org/10.1016/j.jsamd.2020.01.007
55. Deng F, Liu L, Li Z, and Liu J. 3D printed Ti_6Al_4V bone scaffolds with different pore structure effects on bone ingrowth. J Biol Eng. 2021;15(1). https://doi.org/10.1186/s13036-021-00255-8
56. Yang S, Leong K, Du Z, and Chua C. The design of scaffolds for use in tissue engineering. Part I. Traditional factors. Tissue Eng. 2001;7(6):679–89. https://doi.org/10.1089/107632701753337645
57. Mukasheva F, Adilova L, Dyussenbinov A, Yernaimanova B, Abilev M, and Akilbekova D. Optimizing scaffold pore size for tissue engineering: insights across various tissue types. Frontiers Media SA; 2024. https://doi.org/10.3389/fbioe.2024.1444986
58. Salgado AJ, Coutinho OP, and Reis RL. Bone tissue engineering: state of the art and future trends. Macromol Biosci. 2004;4(8):743–65. https://doi.org/10.1002/mabi.200400026
59. Malda J, Klein TJ, and Upton Z. The roles of hypoxia in the in vitro engineering of tissues. Tissue Eng. 2007;13(9):2153–62. https://doi.org/10.1089/ten.2006.0417
60. Innocentini MDM, Faleiros RK, Pisani R, Thijs I, Luyten J, and Mullens S. Permeability of porous gelcast scaffolds for bone tissue engineering. J Porous Mater. 2009;17:615–27. https://doi.org/10.1007/s10934-009-9331-2
61. Osterhoff G, Morgan EF, Shefelbine SJ, Karim L, McNamara LM, and Augat P. Bone mechanical properties and changes with osteoporosis. Injury. 2016;47:S11–S20. https://doi.org/10.1016/S0020-1383(16)47003-8
62. Nauman EA, Fong KE, and Keaveny TM. Dependence of intertrabecular permeability on flow direction and anatomic site. Ann Biomed Eng. 1999;27(4):517–24. https://doi.org/10.1114/1.195
63. Grimm MJ, Williams JL. Measurements of permeability in human calcaneal trabecular bone. J Biomech. 1997;30(7):743–45. https://doi.org/10.1016/S0021-9290(97)00016-X
64. Rathore SS, Mehta B, Kumar P, and Asfer M. Flow characterization in triply periodic minimal surface (TPMS)-based porous geometries: part 1—hydrodynamics. Transp Porous Media. 2023;146(3):669–701. https://doi.org/10.1007/s11242-022-01880-7

How to cite this article: Gabrieli R, Schiavi A, Pennecchi FR, Alidoost D, Schwentenwein M, D'Andrea L, et al. Permeability and microstructural parameters of 3D-printed triply periodic minimal surface (TPMS) hydroxyapatite scaffolds. J Am Ceram Soc. 2025;108:e70104. https://doi.org/10.1111/jace.70104